Structure and Kinetics of Phosphonopyruvate Hydrolase from *Voriovorax* sp. Pal2: New Insight into the Divergence of Catalysis within the PEP Mutase/Isocitrate Lyase Superfamily[†,‡]

Celia C. H. Chen,[§] Ying Han,[||] Weiling Niu,[||] Anna N. Kulakova,[#] Andrew Howard,[⊥] John P. Quinn,[#] Debra Dunaway-Mariano,[||] and Osnat Herzberg[§]

Center for Advanced Research in Biotechnology, University of Maryland Biotechnology Institute, Rockville, Maryland 20850, Department of Chemistry, University of New Mexico, Albuquerque, New Mexico 87131, Biological, Chemical, and Physical Science Department, Illinois Institute of Technology, Chicago, Illinois 60616, and School of Biology and Biochemistry, Medical Biology Centre, The Queens's University of Belfast, Belfast BT9 7BL, Northern Ireland

Received June 17, 2006; Revised Manuscript Received July 26, 2006

ABSTRACT: Phosphonopyruvate (P-pyr) hydrolase (PPH), a member of the phosphoenolpyruvate (PEP) mutase/isocitrate lyase (PEPM/ICL) superfamily, hydrolyzes P-pyr and shares the highest sequence identity and functional similarity with PEPM. Recombinant PPH from *Variovorax* sp. Pal2 was expressed in *Escherichia coli* and purified to homogeneity. Analytical gel filtration indicated that the protein exists in solution predominantly as a tetramer. The PPH pH rate profile indicates maximal activity over a broad pH range.The steady-state kinetic constants determined for a rapid equilibrium ordered kinetic mechanism with Mg^{+2} binding first (K_d =140 ± 40 μM), are k_{cat} = 105 ± 2 s^{-1} and P-pyr K_m = 5 ± 1 μM. PEP (slow substrate $k_{cat} = 2 \times 10^{-4}$ s^{-1}), oxalate, and sulfopyruvate are competitive inhibitors with K_i values of 2.0 ± 0.1 mM, 17 ± 1 μM, and 210 ± 10 μM, respectively. Three PPH crystal structures have been determined, that of a ligand-free enzyme, the enzyme bound to Mg^{2+} and oxalate (inhibitor), and the enzyme bound to Mg^{2+} and P-pyr (substrate). The complex with the inhibitor was obtained by cocrystallization, whereas that with the substrate was obtained by briefly soaking crystals of the ligand-free enzyme with P-pyr prior to flash cooling. The PPH structure resembles that of the other members of the PEPM/ICL superfamily and is most similar to the functionally related enzyme, PEPM. Each monomer of the dimer of dimers exhibits an $(\alpha/\beta)_8$ barrel fold with the eighth helix swapped between two molecules of the dimer. Both P-pyr and oxalate are anchored to the active site by Mg^{2+}. The loop capping the active site is disordered in all three structures, in contrast to PEPM, where the equivalent loop adopts an open or disordered conformation in the unbound state but sequesters the inhibitor from solvent in the bound state. Crystal packing may have favored the open conformation of PPH even when the enzyme was cocrystallized with the oxalate inhibitor. Structure alignment of PPH with other superfamily members revealed two pairs of invariant or conservatively replaced residues that anchor the flexible gating loop. The proposed PPH catalytic mechanism is analogous to that of PEPM but includes activation of a water nucleophile with the loop Thr118 residue.

Organophosphonates are synthesized as secondary metabolites in certain prokaryotes to function as antibiotics and in a wide variety of lower eukaryotes to fulfill specialized roles in pathogenesis or signaling (*1*−*6*). The P−C bond, which replaces the phosphoryl P−O bond of the more common organophosphates, provides both chemical and biochemical stability (*1*). Phosphonate metabolites are ultimately derived from phosphonopyruvate (P-pyr)[1], which in turn is formed from phosphoenolpyruvate (PEP) by the action of PEP mutase (PEPM) (Figure 1) (*7*−*9*). P-pyr formation is thermodynamically unfavorable (*10*, *11*), and therefore, the mutase-catalyzed reaction must be coupled to an exothermic reaction en-route to the phosphonate natural product. 2-Aminoethylphosphonate (AEP), an especially abundant and ubiquitous natural phosphonate (*12*−*17*), is formed by coupling the conversion of PEP to P-pyr with the decarboxylation of the P-pyr to phosphonoacetaldehyde and subsequent transamination to AEP (*8*, *18*). In lower eukaryotes, P-pyr can also undergo transamination to 2-amino-3-phosphonopropionate (phosphonoalanine) (*19*, *20*).

Organophosphonates are degraded by opportunistic soil-dwelling bacteria via the nonspecific C−P lyase pathway, which recovers the phosphorus as orthophosphate (*21*−*25*),

[†] This work was supported by NSF Grant MCB9813271 (to O.H.) and NIH Grant RO1GM36260 (to D.D.-M.).

[‡] The coordinates have been deposited in the Protein Data Bank, entry codes 2hrn (apo enzyme, 2dua (enzyme/oxalate complex), 2hjp (enzyme/phosphonopyruvate complex).

* Corresponding author. Tel: 240-314-6245. Fax: 240-314-6255. E-mail: osnat@carb.nist.gov.

[§] University of Maryland Biotechnology Institute.

[||] University of New Mexico.

[⊥] Illinois Institute of Technology.

[#] The Queens's University of Belfast.

[1] Abbreviations: P-pyr, phosphonopyruvate; PEP, phosphoenolpyruvate; AEP, 2-aminoethylphosphonate; PPH, phosphonopyruvate hydrolase; PEPM, PEP mutase; ICL, isocitrate lyase; MICL, 2-methylisocitrate lyase.

10.1021/bi061208l CCC: $33.50
Published on Web 09/01/2006

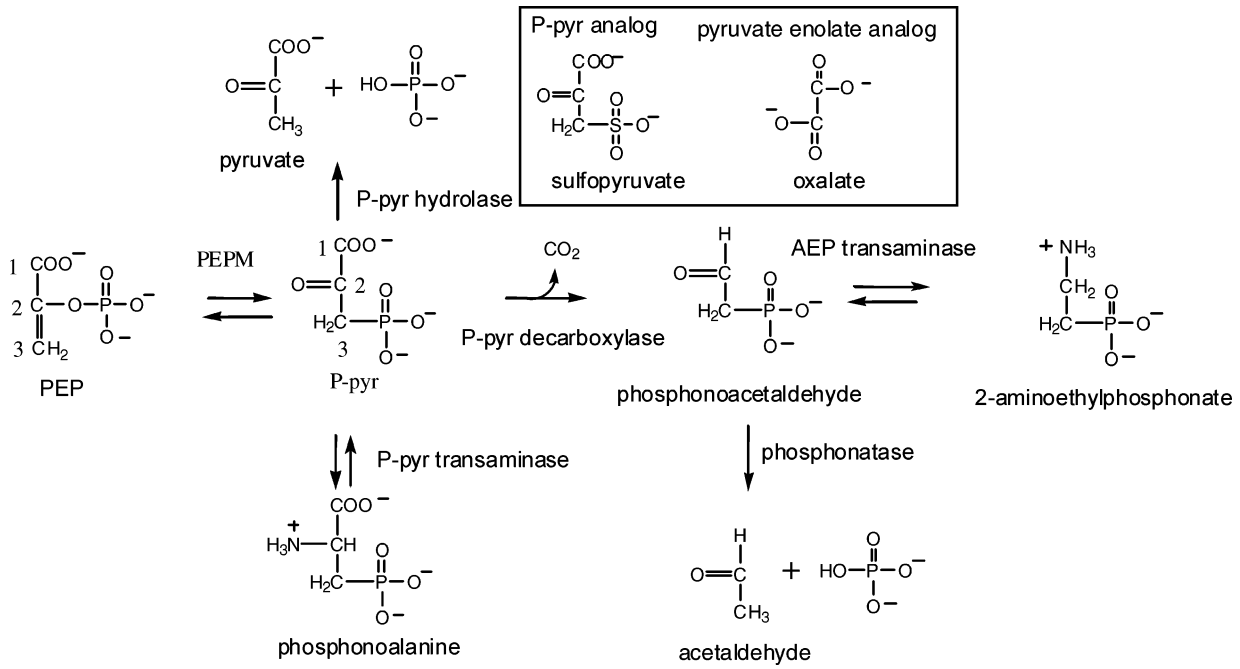

FIGURE 1: P-pyr metabolism. The compounds shown in the box represent the P-pyr and pyruvate enolate analogues, sulfopyruvate and oxalate, respectively, used as ligands for cocrystallization with the PPH.

or by specialized aminophosphonate-degrading pathways that have evolved to recover carbon, phosphorus, and nitrogen (*26*−*30*). The most common of these pathways converts AEP to phosphonoacetaldehyde via transamination of pyruvate to alanine with AEP transaminase (*31*, *32*) and then to acetaldehyde and orthophosphate with phosphonatase (*28*), a member of the HAD enzyme superfamily (*33*) (Figure 1). Alternatively, in some systems, phosphonoacetaldehyde may be oxidized to phosphonoacetate for hydrolysis to acetate and orthophosphate by the enzyme phosphonoacetate hydrolase (*34*, *35*), a member of the alkaline phosphatase superfamily (*36*) (Figure 1). Phosphonoalanine is degraded by conversion to P-pyr (*37*−*39*), which in turn is hydrolyzed by phosphonopyruvate hydrolase (PPH) (*37*, *38*), the topic of this article.

PPH activity was first detected in the cell-free extracts of *Burkholderia cepacia* Pal16, an environmental isolate capable of mineralizing phosphonoalanine (*37*, *39*). PPH evolved to allow opportunistic bacteria to use environmental phosphonoalanine as an alternate source of carbon, nitrogen, and phosphorus. PPH was later purified from the soil isolate *Variovorax* sp. Pal2 (*38*). Remarkably, a BLAST search (*40*) of gene data banks using the *Variovorax* sp. Pal2 sequence (*38*) as query identifies *B. cepacia* Pal16 as the only other deposited PPH sequence.

The *Variovorax* sp. Pal2 and *B. cepacia* PPH share 86% sequence identity with one another and 40% sequence identity with PEPM from *Mytilus edulis*. Both enzymes belong to the PEPM/isocitrate lyase (ICL) superfamily. Members of this superfamily share an $(\alpha/\beta)_8$-barrel fold with a swapped eighth helix first described for the *M. edulis* PEPM (*41*). The α/β barrel framework supports a conserved catalytic scaffold in which the active site signature residues are located on the *C*-terminal side of the β-strands and on a segment following the swapped helix contributed by the adjacent subunit of the homotetramer. In particular, one of the α/β barrel loops undergoes conformational changes from an open or disordered conformation in the unbound state to a conformation that sequesters the active site from bulk solvent upon ligand binding (*41*−*45*). Given the high sequence identity between PEPM and PPH, and the similarity in the two reactions that they catalyze (Figure 1), it is conceivable that the hydrolase evolved from the mutase.

In this article, we report the structure and properties of recombinant PPH from *Variovorax* sp. Pal2 expressed in *E. coli*. The X-ray structure of apo PPH and the complexes PPH/Mg^{+2}−P-pyr and PPH/Mg^{+2}−oxalate are analyzed in the context of the known structures of PEPM/Mg^{+2}−sulfopyruvate and PEPM/Mg^{+2}−oxalate (*41*, *43*). In addition, the biochemical properties of the recombinant PPH (quaternary structure, substrate and metal cofactor specificity, and pH rate profile) are compared to those of PEPM. The results are interpreted as evidence that PPH and PEPM are close relatives that might have diverged in function primarily through mutagenesis of the active site gating loop.

MATERIALS AND METHODS

Preparation of Recombinant Variovorax sp. Pal2 PPH and the PPH R188A Mutant. The PPH gene (EMBL accession number AY179862) was amplified using the PPH-pUC18 clone reported previously (*38*) as template in conjunction with *Pfu* Turbo DNA polymerase and oligonucleotide primers. The PCR product obtained from 25 cycles of denaturation at 94 °C (1 min), annealing at 45 °C (1 min), and elongation at 72 °C (2 min) plus initial denaturation at 94 °C (2 min) and final extension at 72 °C (10 min) was purified by electrophoresis and trimmed using *Nde*I and *Bam*HI restriction enzymes prior to ligation to a *Nde*I- and *Bam*HI-cut pET3c vector (Novagen). The resulting clone, named PPH-pET3c, was used to transform *E. coli* BL21-(DE3) competent cells (Novagen). The cloned plasmid was prepared using a QIAprep Spin Miniprep Kit (QIAGEN), and the gene sequence was verified by DNA sequencing carried out at the Center for Genetics in Medicine, University

of New Mexico School of Medicine, Albuquerque, NM. For protein purification, the *E. coli* cells were grown with mixing (180 rpm) at 25 °C in 2 × 2 L Luria broth (LB) media containing 50 μg/mL carbenicillin to OD_{600nm} ~0.8. Following a 4 h induction period with 0.4 mM isopropyl-β-D-thiogalactopyranoside (IPTG), the cells were harvested by centrifugation at 6500 rpm for 15 min at 4 °C in a yield of 2 g/L of culture media. The cell pellet (9 g) was suspended in 100 mL of ice-cold lysis buffer consisting of 50 mM K^+ HEPES (pH 7.5), 1 mM EDTA, 1 mM benzamide hydrochloride, 0.05 mg/mL trypsin inhibitor, 1 mM 1, 10-phenanthroline, 0.1 mM PMSF, and 5 mM DTT and then passed through a French Press at 1200 PSI. The cell lysate was centrifuged at 4 °C for 60 min at 20 000 rpm (48 384*g*). The supernatant was collected and fractionated by ammonium sulfate induced protein precipitation. The 50−70% ammonium sulfate protein precipitate was dialyzed at 4 °C against 3 × 1 L buffer A (50 mM triethanolamine (pH 7.5) containing 5 mM $MgCl_2$ and 0.5 mM DTT) before loading onto a 4 × 50 cm DEAE-Sepharose column equilibrated with 2 L of buffer A. The column was washed with 1 L of buffer A and then eluted with a 2 L linear gradient of 0 to 0.5 M KCl in buffer A. The PPH-containing fractions (eluted at ~0.3 M KCl) were combined and mixed with ammonium sulfate to 25% saturation. The resulting solution was loaded onto a 3 cm × 30 cm Butyl-Sepharose column equilibrated with 25% ammonium sulfate in buffer A. The column was eluted with 500 mL of 25% ammonium sulfate in buffer A followed by a 1 L linear gradient of 25% to 0% ammonium sulfate in buffer A. The desired protein fractions (eluted at ~11% ammonium sulfate) were combined, concentrated to 15 mL using an Amicon concentrator (Amicon), dialyzed against 4 × 1 L buffer A, and then to 18.6 mg/mL using MACROSEP 10K OMEGA (centrifugation 6500 rpm). The purified protein (yield 10 mg/gm wet cells) was shown to be homogeneous by SDS−PAGE analysis and stored frozen at −80 °C without significant loss of activity.

The R188A PPH mutant gene was prepared using a PCR-based strategy (*46*) with commercial primers and the PPH-pET3C clone as the template. The mutant plasmid was isolated from transformed JM109 *E.coli* host cells, subjected to DNA sequencing to verify the correct gene sequence, and then used to transform BL21(DE3) *E. coli* cells for expression. The PPH R188A mutant protein was purified using the same protocol as that described for the wild-type recombinant enzyme and was shown to be homogeneous by SDS−PAGE analysis.

Molecular Mass Determination. The theoretical subunit molecular mass of recombinant PPH was calculated from the amino acid composition, derived from the gene sequence, by using the EXPASY Molecular Biology Server program Compute pI/MW (*47*). The subunit size was determined by SDS−PAGE analysis with molecular mass standards from Invitrogen, and the subunit mass was determined by MS-ES mass spectrometry (University of New Mexico Mass Spectrometry Lab). The molecular size of native recombinant PPH was determined using gravity flow gel filtration techniques. PPH was chromatographed at 4 °C on a calibrated (Pharmacia Gel Filtration Calibration Kit) 1.5 × 180 cm Sephacryl S-200 column (Pharmacia) using buffer B (25 mM K^+HEPES, 0.15 M KCl, 0.5 mM DTT, at pH 7.5), at a flow rate of 1 mL/min, as the eluant. The molecular mass was determined on the basis of elution volume from a plot of log(molecular mass) of a standard protein versus elution volume.

Crystallization. PPH crystals in the unbound state and in complex with Mg^{2+} and the inhibitor oxalate were obtained by the vapor diffusion method in hanging drops, using equal volumes of protein and reservoir solutions in the drops. The reservoir solution contained 0.1 M K^+HEPES (pH 7.0) and 1.8−2.4 M xylose. The protein sample (at a concentration range of 3.5−11 mg/mL) contained 18 mM triethanolamine (adjusted to pH 7.5 with HCl), 0.18 mM DTT, and 1.8 mM $MgCl_2$. For the crystallization of the PPH/Mg^{2+}−oxalate complex, 8.3 mM of $MgCl_2$ and oxalate were added to the protein sample. Clear lath-shaped crystals with the longest dimension up to 0.5 mm were obtained within two weeks for the PPH/Mg^{2+}−oxalate complex and 4 weeks for the apo enzyme.

For data collection, the crystals were mounted in cryo-loops, with xylose (at a concentration higher than 2.0 M) in the mother liquor serving as the cryoprotectant. The crystals were flash-cooled in liquid propane cooled by liquid nitrogen. The crystals belong to space group *I*222, with one protein molecule per asymmetric unit, and they diffract X-rays to a resolution of approximately 2 Å.

Heavy atom derivative screening using polyacrylamide gel electrophoresis (*48*) established samarium acetate as a candidate for isomorphous replacement. Crystals grown in Mg^{2+}-oxalate solutions were soaked at room temperature for approximately 10 min (*49*) in a solution containing 100 mM samarium acetate, 90 mM K^+HEPES (pH 7.0), and 2.3 M xylose. The soaked crystals were mounted in cryo-loops and flash-cooled in liquid propane.

For the PPH/Mg^{2+}−P-pyr complex, crystals of the ligand-free enzyme were soaked at room temperature for approximately 5 min in 20 μL of saturated P-pyr in 9 mM K^+HEPES (pH 7.0), 50 mM $MgCl_2$, and 2.25 M xylose. The amount of P-pyr constituted an ~5 × 10^5-fold excess of substrate over protein, and with a k_{cat} value of 105 s^{-1} (see Results and Discussion), this excess allowed saturation with substrate for over an hour, guaranteeing full occupancy of the active site over the duration of the soaking period.

X-ray Data Collection. Diffraction data were collected at 100 K. Single wavelength anomalous diffraction (SAD) data at the wavelength of the Sm absorption edge peak were collected on the IMCA-CAT 17-ID beamline equipped with a Mar-CCD detector, at the Advanced Photon Source (Argonne National Laboratory). Data for the PPH/Mg^{2+}−oxalate complex and apo-PPH were collected at 1.000 Å on the IMCA-CAT 17-BM beamline equipped with a Mar-CCD detector. The data were processed with HKL2000 (*50*). The data set for the PPH/Mg^{2+}−P-pyr complex was collected on the home X-ray facility comprising a MicroMax-007 rotating anode generator equipped with an R-AXIS IV^{++} detector (Rigaku/MSC). The data were processed with CrystalClear/d*TREK (Rigaku/MSC). Statistics for data processing are provided in Table 1.

Structure Determination. Molecular Replacement using the AMORE program (*51*) with the PEPM structure (*41*) as the search model yielded a clear solution. However, the electron density map was difficult to interpret in places, and therefore, in parallel, the structure was determined by the Single Isomorphous Replacement Anomalous Scattering method

Table 1: Data Collection and Refinement Statistics.

sample	WT[a]	Sm[a]	Oxa[a]	P-pyr[a]
space group	*I*222	*I*222	*I*222	*I*222
cell dimension (Å)	$a = 74.8$	$a = 74.8$	$a = 74.9$	$a = 74.8$
	$b = 78.6$	$b = 79.2$	$b = 79.2$	$b = 79.1$
	$c = 93.7$	$c = 93.2$	$c = 93.4$	$c = 93.4$
no. of molecules in the asymmetric unit	1	1	1	1
data statistics				
wavelength (Å)	1.0000	1.8438	1.0000	1.5412
resolution (Å)	2.20	2.10	2.00	1.82
no. of observed reflections	67482	114998	137885	161916
no. of unique reflections	13871	16540	19146	24981
completeness (%)[b]	95 (96.)	100(99)	100(99)	99(93)
R_{merge} [b,c]	0.080 (0.656)	0.085 (0.165)	0.070 (0.256)	0.073(0.472)
R_{merge_ano} [b,d]		0.062 (0.140)		
$\langle I/\sigma \rangle$[b]	13.2(1.9)	32.5(12.6)	31.9(14.3)	8.0(2.6)
refinement statistics				
resolution	2.20		2.00	1.90
R_{cryst} [b,e]	0.203		0.155	0.174
R_{free} [b,e]	0.265		0.218	0.226
rmsd bond length	0.021		0.020	0.022
rmsd bond angles	2.0		1.8	2.0

[a] Abbreviations: WT, Mg^{2+}-containing wild-type enzyme; Sm, enzyme/Mg^{2+}-oxalate complex soaked with samarium acetate; Oxa, enzyme/Mg^{2+}-oxalate complex; P-pyr, Mg^{2+}-containing wild-type enzyme crystal soaked with P-pyr. [b] The values in parentheses are for the highest resolution shell: WT, 2.2−2.3 Å; Sm, 2.2−2.1 Å; Oxa, 2.0−2.1 Å; and P-pyr, 1.89−1.82 Å. [c] $R_{merge} = \Sigma_{hkl} [(\Sigma_j | I_j - \langle I \rangle |)/\Sigma_j | I_j |]$. [d] R_{merge_ano} (%) $= \Sigma_{hkl} [(\Sigma_j | I_j - \langle I \rangle |)/\Sigma_j | I_j |]$, with Bijvoet pairs separated. [e] $R_{cryst} = \Sigma_{hkl} | |F_o| - |F_c| |/\Sigma_{hkl} |F_o|$, where F_o and F_c are the observed and calculated structure factors, respectively. R_{free} refers to 5% of all reflections not refined.

(SIRAS). The PPH/Mg^{2+}−oxalate data were used as the reference set, and the Sm-soaked PPH/Mg^{2+}−oxalate data as the derivative set. An Sm site was identified in the difference Patterson map, which in retrospect coincided with the active site Mg^{2+}.

Phases were calculated with Solve (*52*), and modified with Resolve (*53*, *54*). Resolve automated model building (*55*) identified 193 out of a total of 290 residues (67% of the polypeptide chain). With the Molecular Replacement model as a guide, the main chain atoms of another 41 residues were identified. Five additional residues were built manually using the computer graphics program Turbo-Frodo (*56*).

Structure Refinement. The PPH/Mg^{2+}−oxalate model was refined using the CNS program (*57*). One cycle of simulated annealing molecular dynamics at 2500 K was followed by alternating positional and individual temperature factor refinement cycles. Maximum likelihood refinement was used (*58*). The resulting models were inspected and modified using Turbo-Frodo (*56*). As the electron density improved, additional residues were traced. Mg^{2+} and oxalate were added to the model. Water molecules were selected automatically in the difference Fourier map using 3σ cutoff criteria. A xylose molecule, a sodium ion, and two half-occupancy chloride ions (located on 2-fold crystallographic symmetry axis) were added at the last stage of refinement. The two chloride ions, the sodium ion, and a symmetry related sodium ion form a squared cluster. The final model includes 283 amino acid residues, 343 water molecules, 1 magnesium ion, 1 oxalate ion, 1-sodium ion, 2 chloride ions, and 1 xylopyranoside molecule. Table 1 provides the refinement statistics.

The structures of apo PPH and that of the PPH/Mg^{2+}−P-pyr complex were refined using the Mg^{2+}-oxalate bound protein structure as the initial model. The density for the P-pyr and Mg^{2+} was exceptionally well defined. The final model of the free enzyme includes 281 amino acid residues, 183 water molecules, a sodium ion, and 2 chloride ions; the final model of the enzyme/substrate complex includes 283 amino acid residues, 197 water molecules, 1 magnesium ion, 1 P-pyr molecule, 1 sodium ion, 2 chloride ions, and 1 xylopyranoside molecule (Table 1).

Steady-State Kinetic Constant Determination. The steady-state kinetic parameters (K_m and k_{cat}) for reactions catalyzed by PPH were determined from the initial velocity data measured as a function of P-pyr concentration (ranging from $0.5K_m$ to $5K_m$). The 1 mL of reaction solutions contained 3 nM PPH, varying concentrations of P-pyr, 5 mM $MgCl_2$, 0.2 mM NADH, and 20 units/mL lactate dehydrogenase in 50 mM K^+HEPES buffer (pH 7.5, 25 °C). Reactions were monitored at 340 nm ($\Delta\epsilon = 6.2$ mM^{-1} cm^{-1}). The initial velocity data were fitted to eq 1 with KinetAsystI

$$V_0 = V_{max}[S]/(K_m + [S]) \quad (1)$$

where [S] is the substrate concentration, V_0 is the initial velocity, V_{max} is the maximum velocity, and K_m is the Michaelis−Menten constant for the substrate. The k_{cat} value was calculated from V_{max} and the enzyme concentration using the equation $k_{cat} = V_{max}/[E]$, where [E] is the protein subunit molar concentration in the reaction calculated from the ratio of measured protein concentration and the protein molecular mass (31179 Da). The initial velocity data were measured as a function of the reaction pH by using the following buffers at the indicated pH values: 50 mM MES and 50 mM HEPES (pH 6.0−8.0), and 50 mM HEPES and 50 mM TAPS (pH 8.0−9.1).

All known PPH inhibitors are competitive inhibitors. The competitive inhibition constant, K_i, was determined for PEP, sulfopyruvate, and oxalate. The 1 mL reaction mixtures contained 50 mM K^+HEPES, 5 mM $MgCl_2$, varying concentrations of P-pyr (0.5−10 K_m), PPH (3.4 nM for oxalate

Table 2: Michaelis Constant (K_m) for the Metal Ion Activator and Maximum Velocity (V_m) (Standardized to V_m for Mg^{2+}Activation)[a]

	activator K_m (μM)			M^{2+} V_m/ $Mg^{2+}V_m$		
metalactivator	PPH	PEPM *M. edulis*	PEPM *T. pyriformis*	PPH	PEPM *M. edulis*	PEPM *T. pyriformis*
Mg^{2+}	3.5 ± 0.3	4	5	1.0	1.0	1.0
Co^{2+}	6.1 ± 0.7	0.3	2	2.8	0.7	0.5
Mn^{2+}	0.73 ± 0.03	0.1	7	0.4	0.3	0.3
Zn^{2+}	not active	0.2	7	no active	0.5	0.4
Ca^{2+}	not active	not active	not active	not active	not active	not active

[a] The values were measured for *Variovorax* sp. Pal2 PPH catalyzed hydrolysis of 1 mM phosphonopyruvate in 50 mM K^+HEPES (pH 7.5, 25 °C). See the Materials and Methods section for details. Kinetic values previously measured for *Mytilus edulis* PEP mutase (*59*) and *Tetrahymena* PEP mutase (*60*) are for catalyzed conversion of 0.1 mM phosphonopyruvate to PEP in 50 mM K^+HEPES (pH 7.5, 25 °C). Not active is defined as no activity above background, which corresponds to a detection limit of 1×10^{-4} s^{-1}.

and sulfopyruvate, 5 nM for PEP), 0.2 mM NADH, 20 units/mL lactate dehydrogenase and three concentrations of PEP (0, 1.5 and 4 mM), sulfopyruvate (0, 200, and 400 μM), or oxalate (0, 20 and 40 μM). Initial velocities were measured at 340 nm ($\Delta\epsilon$ = 6.2 mM^{-1} cm^{-1}), and the competitive inhibition constant K_i was determined by fitting initial velocity data to eq 2 with KinetAsystI

$$V_0 = V_{max}[S]/(K_m(1 + ([I]/K_i)) + [S]) \quad (2)$$

where [I] is the inhibitor concentration.

Screening of Alternatives Substrate. PPH (35.4 μM) catalyzed hydrolysis of 5 mM PEP, sulfopyruvate or phosphonoacetaldehyde in 1 mL of 50 mM K^+HEPES (pH 7.5, 25 °C) containing 5 mM $MgCl_2$, 0.2 mM NADH, and 20 units/mL lactate dehydrogenase was monitored at 340 nm ($\Delta\epsilon$ = 6.2 mM^{-1} cm^{-1}) for 30 min. The k_{cat} was calculated from the equation $k_{cat} = V_{max}/[E]$ by assuming that the initial velocity measured for each reaction estimated the V_{max}.

Metal Ion Activation and Inhibition of PPH. The metal ion-free PPH was prepared by several 3 h dialyses against 500 mL of 30 mM EDTA, 50 mM triethanolamine, and 0.5 mM DTT (pH 7.5, 4 °C) followed by several 3 h dialyses against 500 mL of 50 mM triethanolamine and 0.5 mM DTT (pH 7.5, 4 °C). The velocity of pyruvate formation in reaction solutions containing 3.7 nM PPH, 1 mM P-pyr, 20 units/mL lactate dehydrogenase, 0.2 mM NADH, and varying concentrations of $MgCl_2$, $MnCl_2$, $CoCl_2$, $CaCl_2$, and $ZnCl_2$ in 50 mM K^+HEPES buffer (pH 7.5, 25 °C), was monitored at 340 nm ($\Delta\epsilon$ = 6.2 mM^{-1} cm^{-1}). The initial velocity data were analyzed using eq 1 with KinetAsystI. The K_i for Ca^{2+} was determined by measuring the initial velocity of pyruvate formation in reaction solutions containing 4 nM PPH, 0.2 mM phosphonopyruvate, 20 units/mL lactate dehydrogenase, 0.2 mM NADH, varying concentration of $MgCl_2$ (10−200 μM) and using three fixed concentration of $CaCl_2$ (0, 30, and 60 μM) in 50 mM K^+HEPES buffer (pH 7.5, 25 °C). Data fitting to eq 2 was carried out with KinetAsystI. The kinetic mechanism was determined by measuring the initial velocity of the PHH catalyzed hydrolysis of P-pyr as a function of the concentration of both Mg^{+2} and P-pyr ([A] and [B], respectively). Data were fitted to eq 3 with KinetAsystI

$$V_0 = V_{max}[A][B]/(K_B[A] + [A][B] + K_{iA}K_B) \quad (3)$$

where K_{iA} is the Mg^{+2} dissociation constant and K_B is the P-pyr Michaelis constant.

Determination of pH-Rate Profiles for Phosphonopyruvate Hydrolase Catalysis. The initial velocity data were measured as a function of the reaction pH by using the following buffers at the indicated pH values: 50 mM MES and 50 mM HEPES (pH 5.6−8.0), 50 mM HEPES and 50 mM TAPS (pH 8.0−9.1), and 50 mM TAPS and 50 mM CAPSO (pH 9.1−9.6). The k_{cat} and k_{cat}/K_m values were determined as described in the previous section.

RESULTS AND DISCUSSION

Physical and Catalytic Properties of PPH. Recombinant *Variovorax* sp. Pal2 PPH was purified to homogeneity by using a column chromatography based protocol in an overall yield of 10 mg/g wet cells. The theoretical molecular mass of PPH calculated from the amino acid sequence is 31179 Da, which agreed with the experimental molecular mass of 31179 Da measured by mass spectral techniques. The subunit size of PPH estimated by SDS−PAGE analysis is 31 kDa, whereas the native protein size determined by gel filtration chromatography is ∼110 kDa. This result is consistent with the homotetrameric quaternary structure observed by X-ray crystallography (see below). PPH's closest sequence homologue, PEPM, is also a tetramer both in solution and in the crystal form (*41*, *43*, *59*).

The steady-state kinetic constants for metal ion activation of PPH at pH 7.5 and 25 °C were determined at a saturating concentration of P-pyr (1 mM) and varying metal ion concentration. The results are presented in Table 2 along with previously published metal activation constants measured for the PEPM from *M. edulis* and *Tetrahymena pyriformis* (*59*, *60*). Ca^{2+} did not activate PPH or PEPM, but was instead shown to be a competitive inhibitor (vs Mg^{2+}) of PPH with a K_i = 32 ± 3 μM. Zn^{2+} is an effective activator of PEPM, but it did not activate PPH. Mg^{2+}, Mn^{2+}, and Co^{2+} are efficient activators of both the hydrolase and the mutase.

The kinetic mechanism of PPH was examined by measuring the initial velocity of the reaction as a function of Mg^{2+}-concentration at changing fixed P-pyr concentration. A plot of $1/V_0$ versus $1/[Mg^{2+}]$ determined at 5 different concentrations of P-pyr intersected at the left of the $1/V_0$ axis, whereas a plot of $1/V_0$ versus 1/[P-pyr] determined at 5 different concentrations of Mg^{2+} intersected at the $1/V_0$ axis (data not shown). This pattern is consistent with a rapid equilibrium ordered mechanism in which Mg^{2+} binds first with K_d = 140 ± 40 μM (K_{iA} in eq 3) and P-pyr binds second with K_m = 5 ± 1 μM (K_B in eq 3). This same kinetic mechanism was observed for *T. pyriformis* PEPM with the Mg^{2+} K_d =

Table 3: Comparison of Steady-State Kinetic Constants Measured for PPH with Those Measured for *M. edulis* PEPM and *T. pyriformis* PEPM[a]

		substrate and/or inhibitor			
enzyme	rate constant	P-pyr	PEP	oxalate	sulfopyruvate
PPH (*Vari.*)		Pyr + P_i[f]	Pyr + P_i[f]		
	k_{cat} (s^{-1})	105 ± 2	~2 × 10^{-4}		
	K_m (μM)	19.5 ± 0.9	2000 ± 100		
	K_i (μM)			17 ± 1	210 ± 10
PEPM (*T. pyr*)		PEP[f]	P-pyr[f]		
	k_{cat} (s^{-1})	100[b],150[c]	5[a]		
	K_m (μM)	3.5[b],10[c]	770[a]		
	K_i (μM)		350[c]	32[b],25[b]	not determined
PEPM (*M. ed*)		PEP[f]	P-pyr[f]		
	k_{cat} (s^{-1})	34[d]	not determined		
	K_m (μM)	5.8 ± 0.8[d]	not determined		
	K_i (μM)			8[e]	22[e]

[a] The values in parenthesis are independent measurements. [b] Are taken from ref 11 (*11*). [c] Are taken from ref (*70*). [d] Are taken from ref (*59*). [e] Are taken from ref (*43*). [f] Are the product measured.

300 ± 100 μM and the P-pyr K_m = 2 ± 1 μM (*60*). Kinetic constant determination made at fixed, saturating $MgCl_2$ (5 mM) and varied P-pyr, using eq 1, defined k_{cat} and P-pyr apparent K_m values as listed in Table 3. Conversely, the apparent Mg^{2+} K_m = 3.5 ± 0.3 μM was determined at 1 mM P-pyr (compared to apparent Mg^{2+} K_m = 4 ± 1 μM for *M. edulis* PEPM and apparent Mg^{2+} K_m = 5.8 ± 0.8 μM for *T. pyriformis* PEPM measured at 100 μM P-pyr).

To determine the pH range for optimal PPH catalytic efficiency the k_{cat} and k_{cat}/K_m values were determined (at varying P-pyr concentration and fixed, saturating Mg^{2+} concentration) as a function of the reaction solution pH. The pH rate profiles mirror those previously measured for *T. pyriformis* PEPM (*60*) and show that the efficiency of substrate binding and catalytic turnover are relatively constant over the pH range 6−9. In contrast, the activity of *M. edulis* PEPM is maximal at pH 8, dropping above and below this pH (*59*).

To distinguish the catalytic and ligand-binding properties of PPH from those of PEPM, known substrates and inhibitors of PEPM were tested with PPH. The results are summarized in Table 3. In the physiological direction, PEPM catalyzes the conversion of PEP to P-pyr, yet the solution equilibrium is unfavorable with K_{eq} within the range of 2 and 9 × 10^{-4} (*11*). Furthermore, as the steady-state kinetic constants listed in Table 3 indicate, mutase catalysis is more efficient for the conversion of P-pyr to PEP than it is for the conversion of PEP to P-pyr. PPH and PEPM are similar in both the turnover rate and the K_m value for P-pyr, and neither enzyme binds PEP tightly (Table 3). However, whereas PEPM catalyzes the intramolecular phosphoryl transfer from PEP at a turnover rate of 5 s^{-1}, PPH catalyzes the hydrolysis of PEP at the slow rate of 2 × 10^{-4} s^{-1}. Therefore, it is evident that the PPH active site has evolved to distinguish between PEP and P-pyr as targets for phosphate liberation, as necessary for the conservation of energy production via the glycolytic pathway. Finally, mutase activity of PPH and P-pyr hydrolysis by PEPM were examined carefully and were not detected.

The P-pyr structural analogue sulfopyruvate (shown in Figure 1) is a competitive inhibitor of both PPH and PEPM, yet it binds to PEPM 10-fold more tightly than it does to PPH (Table 3). As discussed below, the gating loop in the current structures of PPH is disordered, which prevents structural interpretation of the discrepancy in sulfopyruvate inhibition rates. Oxalate, an analogue of the putative reaction intermediate pyruvate enolate (Figure 1), binds tightly to both PPH and PEPM (Table 3).

Overall Structure. The close similarity between the three structures of PPH, apo-PPH, PPH/Mg^{2+}−oxalate and PPH/Mg^{2+}-phosphonopyruvate, is reflected by the low root-mean-square deviation (rmsd) value of 0.3 Å over 1200 paired superposed main chain and Cβ atoms. The overall fold of PPH is similar to that of the other members of the ICL/PEPM superfamily: a tetramer consisting of a dimer of dimers (Figure 2A), with each monomer forming an $(\alpha/\beta)_8$ barrel, and the active site located at the *C*-terminal edge of the barrel (identified by the Mg^{+2} cofactor and P-pyr substrate ligand in Figures 2B and C). Two molecules in a dimer swap their barrel's eighth helix (α8) (barrel helix and β-strand numbering 1−8), and each *C*-terminus segment (α9-α11) following the eighth helix (α8) of the barrel traverses the *C*-terminal rim of the barrel of the partner molecule. The *N*-terminal helix, α0, covers the bottom *N*-terminal end of the barrel. There was no electron density associated with amino acid residues 117−126 at the *C*-terminal side of the barrel in all three structures; thus, this region was not modeled and is interpreted as being disordered.

The 2-fold axis, relating the two molecules with swapped helices, runs parallel to the unit cell *a*-axis, and the eight asymmetric units within the cell contain two tetramers, one at the origin and the second at the center of the unit cell. The tetramers obey a 222-symmetry, with the axes of the barrels perpendicular to the crystal's *a*-axis, approximately in the $b + c$ and $b - c$ directions. The *C*-terminal ends of the barrels face the bulk solvent regions. Within a tetramer, the dimer−dimer interactions occur predominantly between the loops at the bottom of the barrels and the α-helices surrounding the barrels.

Only a few contacts occur between tetramers, mediated by the *C*-terminus of α1 of one molecule in a tetramer and the *C*-terminal helix of another molecule in the second tetramer. In addition, an α-D-pyranose xylose molecule bridges two tetramers in the structures of the enzyme/Mg^{2+}−oxalate and enzyme/Mg^{2+}−P-pyr complexes. The xylose molecule was not seen in the electron density map of the apo PPH structure, which was determined at a lower resolution than the structures of the enzyme/ligand complexes.

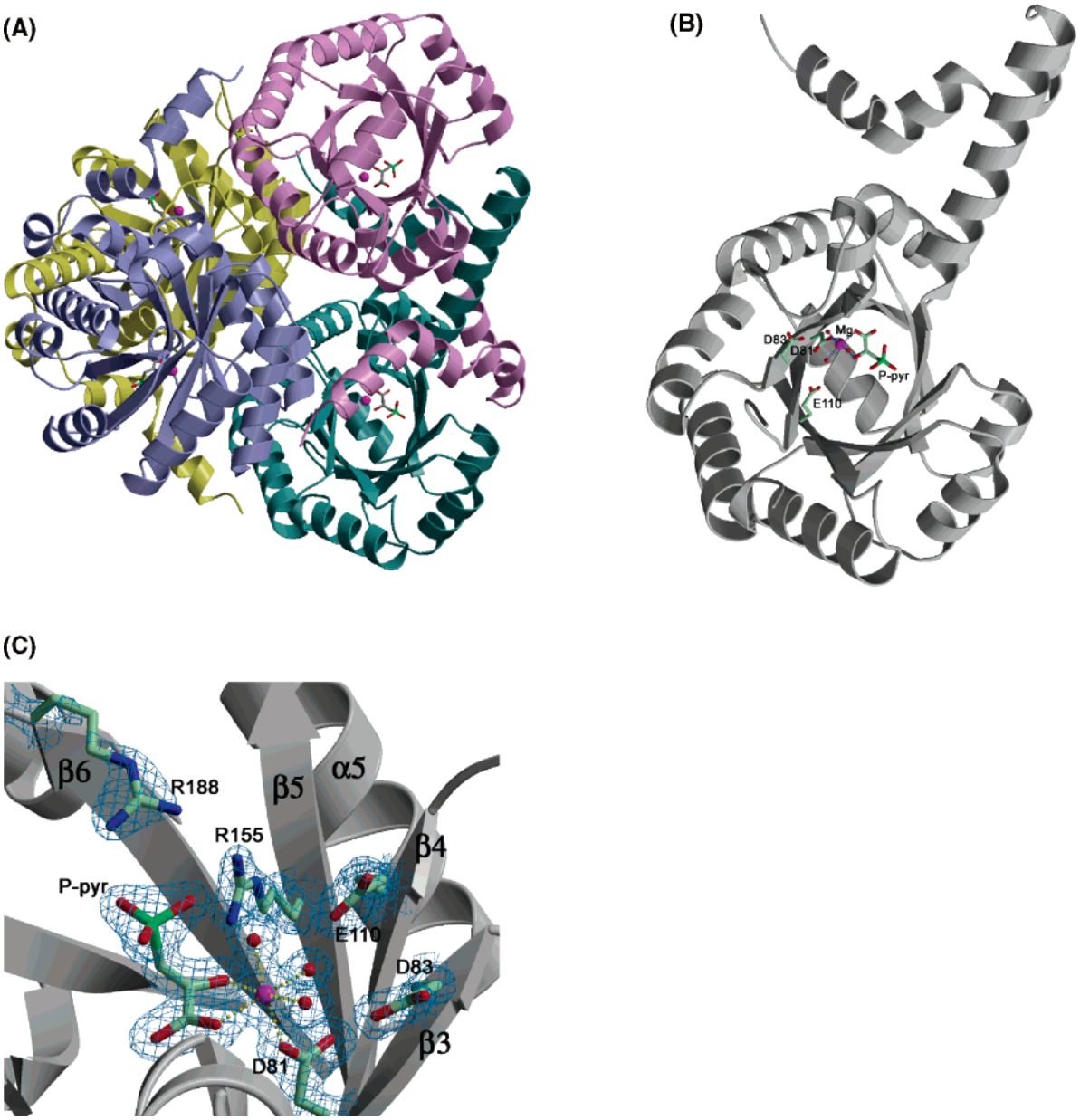

FIGURE 2: Structure of PPH. (A) Ribbon representation of the tetramer. Mg^{2+} is shown as a magenta sphere and P-pyr as a stick model. (B) Ribbon representation of the monomer. In addition to Mg^{2+} and P-pyr, three residues involved in Mg^{2+} coordination are also shown in stick model, and bridging water molecules are depicted as red spheres. (C) PPH active site region including the electron density map associated with P-pyr and surrounding key residues. Coordination of Mg^{2+} is shown in broken yellow lines. The sigma-weighted difference Fourier map is calculated with the coefficients $2F_o - F_c$ and is contoured around the displayed side chains at 1.4σ level. An atomic color scheme is used: red, oxygen; blue, nitrogen; pale green, carbon; bright green, phosphorus; magenta, Mg^{2+}.

Structural Homology with PEPM/ICL Superfamily Members. Of the PEPM/ICL superfamily members, the 3D structure of PPH is most similar to that of *M. edulis* PEPM, consistent with the highest amino acid sequence identity (40%) and the closest functional similarity between the two enzymes. The rmsd value for 279 of the 285 defined Cα atoms of the superimposed *M. edulis* PEPM and PPH structures is 1.1 Å. (The disordered PPH residues 117−126 were excluded.) Structural deviations are restricted to the α-helices and connecting loops. Specifically, helix α6 is shifted approximately 1.5 Å, leading to deviations in the positions of the preceding and following loops. Helix 7 of PPH shifts closer to the barrel and toward the *N*-terminus to accommodate an extra residue in the ensuing loop. The *N*-terminal helix leading to the α/*β* barrel, α0, is further away from the barrel in PPH than in PEPM, whereas the PPH *C*-terminus segment aligns well with that of PEPM.

The flexible active site gating loop characteristic of the PEPM/ICL superfamily (Figure 3) corresponds to residues 117−126 in PPH. Unfortunately, the loop is disordered in each of the three PPH structures. Nevertheless, much can be surmised from the examination of the PEPM loop (*41*, *42*) (Figure 3A) as well as the corresponding loops in ICL (*45*), 2-methylisocitrate lyase (MICL) (*44*), and the petal death protein (a 2-alkyl or 2-hydroxymalate lyase) (*61*). It is known from previous work with PEPM/ICL superfamily members that in the closed conformation, the loop displaces water molecules from the active site and positions loop side chains for substrate binding (PEPM) or acid/base catalysis (the C−C bond lyases) (*42*−*45*, *61*). Catalysis, thus, occurs

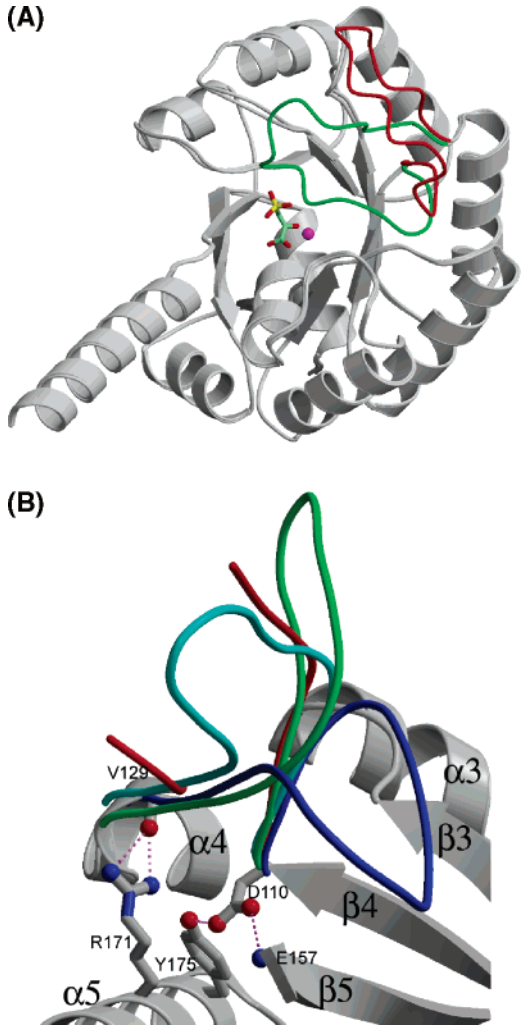

FIGURE 3: Conformational flexibility of the ICL/PEPM superfamily gating loop. (A) Open and closed conformations of the gating-loop in *Mytilus edulis* (adopted from (*42*)). (B) PPH loop's anchoring residues shown in the context of various structures. The gating loops are colored as follows: red, the disordered loop of PPH; blue, the closed loop of PEPM; green, the open loop of ICL (PDB entry code 1MUM); and cyan, the open loop of MICL (PDB entry code 1IGW). Interactions between anchoring residues are highlighted in broken magenta lines.

when the loop closes; however, for the product to dissociate and the substrate to bind, the gating loop must move away to allow access to the active site. Ligand exchange, therefore, occurs from the loop-open conformation. In PEPM, ICL, and MICL, both the loop-open and loop-closed conformations have been observed by X-ray crystallography (*41*−*45*, *61*−*65*). The structures of the central complexes (viz. succinate plus pyruvate for MICL (*44*); nitropyruvate plus glyoxylate for ICL (*45*), and sulfopyruvate for PEPM (*43*)) show the loop-closed conformation, whereas unliganded enzyme or binary complexes display a loop-open conformation or contain a disordered loop segment.

The observation of a disordered gating loop in all three PPH structures, including the one in which the enzyme was cocrystallized with oxalate is curious. Crystal packing could potentially effect the loop conformation; however, the location of four symmetry-related gating-loop roots is within a large solvent channel, and thus, crystal packing does not prevent loop closure. This is mechanistically important because solvation of the active site during catalytic turnover would disrupt the electrostatic environment created through specific orientation of dipoles in a solvent free medium and, therefore, interfere with transition state stabilization (*66*). On the basis of an assumption that catalytic turnover in PPH must occur from the loop-closed conformation and that loop conformation in PPH is defined by crystal packing forces, we searched for evidence that the PPH loop is mechanically competent for closure over the active site. Accordingly, 15 unique crystal structures of complexes of PEPM, ICL, MICL, and the petal death protein were aligned with the structure of the PPH/Mg^{2+}−P-pyr complex using the computer program ALIGN (*67*). From this alignment, it was discovered that the points of loop connection with the β4 and α4 barrel segments are associated with two sets of conserved hydrogen-bonding interactions that alter the main chain conformation and anchor the chain in 3D space. On one side of the PPH barrel (Figure 3B), the α4 Val129 main chain C═O forms a hydrogen bond with the α5 Arg171 side chain. Across the PPH barrel, the β4 Glu110 side chain forms a hydrogen bond with the side chain of α5 Tyr175 and with the main chain NH of β5 Glu157. The structure-based sequence alignment of Figure 4 identifies the residues participating in these loop-defining interactions within other superfamily members.

Catalytic cycling and alternation between loop-open and loop-closed conformations in the PEPM and the C−C bond lyases may be compared with that described for triosephosphate isomerase and dihydrofolate reductase. NMR studies of these enzymes indicate that loop movement is synchronized with the chemical transformation occurring within the active site (*68*, *69*). Hydrogen bond interactions between loop residues and the residues of the active site scaffold and/or bound ligands act to reduce the rate of loop dissociation so that it might be correlated with the rate of substrate turnover. An examination of the loop-closed structures of the ICL/PEPM superfamily reveals common sites of hydrogen interaction between loop residues and specific active site residues. The residues responsible for these interactions are conserved in PPH. First, the PPH loop Lys116 is invariant among the mutases (PEPM and carboxyPEPM) and the C−C bond lyases (ICL, MICL, the petal death protein, and oxaloacetate acetylhydrolase). Loop closure moves the lysine residue from solvent into the active site, where it engages in favorable electrostatic interaction with an invariant active site carboxylate residue (*viz*. Asp83 in PPH). Thus, just as the Lys120−Asp87 ion pair stabilizes the loop-closed conformation in PEPM (Lys142−Asp109 in the petal death protein (*61*); Lys186−Glu162 in ICL (*45*); and Lys121−Asp87 in MICL (*44*)), we expect that the ion pair formation between Lys116 and Asp83 will stabilize the loop-closed conformation in PPH.

In most closed-loop structures, the substrate-binding or acid/base residue of the loop (Asn 122 in PEPM; Cys123 in MICL; Cys191 in ICL; Cys144 in the petal death protein) engages in hydrogen bond interaction with an active site residue and/or the substrate ligand. In the PEPM/Mg^{+2}−oxalate complex, the Asn122 side chain forms a hydrogen bond with the invariant active site Asp58, and in the PEPM/Mg^{+2}−sulfopyruvate complex, the Asn122 side chain forms a hydrogen bond with both Asp58 and the charged sulfo-group of the sulfopyruvate ligand (*41*, *43*). In addition, the hydrophobic loop residue Leu124 desolvates the active site of PEPM and thus enhances the electrostatic environment

```
                        | α0 |        | β1 | | α1 | | β2 || α2 |
PPHA_9burk                MTKNQALRAALDSGR-----LFTAMAAHNPLVAKLAEQAGFGGIWGSGFELSAS  49
PEPM_myted              STKVKKTTQLKQMLNSKD-----LEFIMEAHNGLSARIVQEAGFKGIWGSGLSVSAQ  53
MICL_myctu               SLHSPGKAFRAALTKEN-----PLQIVGTINANHALLAQRAGYQAIYLSGGGVAAG  52
MICL_salty            MASSLHSPGQAFRAALAKEN-----PLQIVGAINANHALLAQRAGYQAIYLSGGGVAAG  52
ICL_ecoli        M(41)ECTLAQLGAAKMWRLLHGESK--KGYINSLGALTGGQALQQAKAGIEAVYLSGWQVAAD  98
ICL_myctu        M(44)EHTLARRGAEVLWEQLHD-L----EWVNALGALTGNMAVQQVRAGLKAIYLSGWQVAG-  97
ICL_emeni        M(47)EYP-SNVQAKKLWGILER-NFKNKEASFTYGCLDPTMVTQMAK-YLDTVYVSGWQSSS- 103

                 |        | α2 |       | β3 |     | α3 |
PPHA_9burk -Y------AVPDANILSMSTHLEMMRAIASTV----SIPLIADIDTGFG-NAVNVHYVVPQYEAA 102
PEPM_myted -L------GVRDSNEASWTQVVEVLEFMSDAS----DVPILLDADTGYG-NFNNARRLVRKLEDR 106
MICL_myctu SL------GLPDLGISTLDDVLTDIRRITDVC----SLPLLVDADIGFGSSAFNVARTVKSMIKA 107
MICL_salty SL------GLPDLGISTLDDVLTDIRRITDVC----PLPLLVDADIGFGSSAFNVARTVKSIAKA 107
ICL_ecoli  --ANLAASMYPDQSLYPANSVPAVVERINNTF(22)FLPIVADAEAGFG-GVLNAFELMKAMIEA 178
ICL_myctu  -DANLSGHTYPDQSLYPANSVPQVVRRINNAL(18)LAPIVADGEAGFG-GALNVYELQKALIAA 174
ICL_emeni  -TASSTDEPSPDLADYPMNTVPNKVNHLWMAQ(27)LRPIIADADTGHG-GLTAVMKLTKLFVER 189

             | β4 || the mobile loop || α4 |       | β5 |
PPHA_9burk GASAIVMEDKTFP-KDTSLRTDGRQELVRIEEFQGKIAAATAAR---ADRDFVVIARVEALIAG- 162
PEPM-myted GVAGACLEDKLFP-KTNSLHDGRAQPLADIEEFALKIKACKDSQ---TDPDFCIVARVEAFIAG- 166
MICL_myctu GAAGLHIEDQVGA-KRCG-HRPN-KAIVSKEEMVDRIRAAVDAK---TDPDFVIMARTDALA-V- 164
MICL_salty GAAALHIEDQVGA-KRCG-HRPN-KAIVSKEEMVDRIRAAVDAR---TDPNFVIMARTDALA-V- 164
ICL_ecoli  GAAAVHFEDQLASVKKCG-HMGG-KVLVPTQEAIQKLVAARLCADVTGV-PTLLVARTDADAAD- 239
ICL_myctu  GVAGSHWEDQLASEKKCG-HLGG-KVLIPTQQHIRTLTSARLAADVADV-PTVVIARTDAEAAT- 235
ICL_emeni  GAAGIHIEDQAPGTKKCG-HMAG-KVLVPISEHINRLVAIRAQADIMGT-DLLAIARTDSEAAT- 250

                 | α5 | | β6 |   | α6 |       | β7 |
PPHA_9burk ------LGQQEAVRRGQAYEEAGADAILIHSRQKTP-DEIL-AFVKSW--P--G-KVPLVLVPT- 213
PEPM-myted ------WGLDEALKRAEAYRNAGADAILMHSKKADP-SDIE-AFMKAW--N--N-QGPVVIVPT- 217
MICL_myctu ------EGLDAAIERAQAYVEAGAEMLFPEA-I--T-E-LA-M-YRQFADA--V-QVPILANITE 213
MICL_salty ------EGLEAALDRAQAYVDAGADMLFPEA-I--T-E-LS-M-YRRFADV--A-QVPILANITE 213
ICL_ecoli  ( 26)HAGIEQAISRGLAYAP-YADLVWCETST-PDLEL-ARRFAQAI--HAKYPGKLLAYNC-- 318
ICL_myctu  ( 26)KNGIEPCIARAKAYAP-FADLIWMETGT-PDLEA-ARQFSEAV--KAEYPDQMLAYNC-- 314
ICL_emeni  (121)QGGTQCAINRAVAYAP-FADLIWMESKL-PDYKQ-AKEFADGV--HAVWPEQKLAYNL-- 424

                              | α7 |   | β8 | | α8 | | --
PPHA_9burk ---A--YPQ-----------LTEADIAALSKVGIVIYGNHAIRAAVGAVREVFARIRRDGGIRE- 261
PEPM_myctu ---K--YYK-----------TPTDHFRDMG-VSMVIWANHNLRASVSAIQQTTKQIYDDQSLVN- 264
MICL_myctu FGAT--PL------------FTTDELRSAH-VAMALYPLSAFRAMNRAAEHVYNVLRQEGTQ-KS 262
MICL_salty FGAT--PL------------FTTDELRSAH-VAMALYPLSAFRAMNRAAEKVYTVLRQEGTQ-KN 262
ICL_ecoli  ---SPSFNWQKNLDDKTIASF-QQQLSDM-GYKFQFITLAGIHSMWFNMFDLANAYAQGEG-MK- 376
ICL_myctu  ---SPSFNWKKHLDDATIAKF-QKELAAM-GFKFQFITLAGFHALNYSMFDLAYGYAQN-Q-MS- 371
ICL_emeni  ---SPSFNWKKAMPRDEQETY-IKRLGAL-GYAWQFITLAGLHTTALISDTFAKAYAKQ-G-MR- 481

           | α9 |              | α10 || α11 |
PPHA_9burk VDA-A-L------------PSVKEIIELQGD-E-RMRA-VEARYLK------------        290
PEPM_myted VED-K-I------------VSVKEIFRLQRD-D-ELVQ-AEDKYLPKN----------        295
MICL_myctu VI--DTM------------QTRNELYESINY-YQY-EEKL-DNLFARSQVK-------        296
MICL_salty VI--DIM------------QTRNELYESINY-YQF-EEKL-DALYRNKKS                300
ICL_ecoli  HYVEKV-QQPEFAAAKDGYTFVSH-QQEV-G-TGYFDKVTTIIQGGTSSVTALTGSTEESQF--  434
ICL_myctu  AYVEL--QEREFAAEERGYTATKH-QREV-G-AGYFDRIATTVDP-NSSTTALTGSTEEGQFH-  428
ICL_emeni  AYGELV-QEPEMANG---VDVVTH-QKWS-G-ANYVDNMLKMITGGVSSTAAMGKGVTEDQFKS  538
```

FIGURE 4: Structure-based multiple sequence alignment of PEPM/ICL superfamily members with known crystal structures. The first column lists the protein name and the second column abbreviates species name: *9burk*, *Variovorax* sp. Pal2; *myted*, *Mytilus edulis*; *myctu*, *Mycobacterium tuberculosis*; *salty*, *Salmonella typhimurium*; *ecoli*, *Escherichia coli*; *emeni*, *Emericella nidulans*. For each block, the residue numbers at the end of the block are listed. Numbers in parentheses indicate how many residues in an insertion are omitted. Structural elements are indicated above the sequence blocks and colored gray for α- helices, yellow for *β*-ribbons, and magenta for the gating loop. Important residues discussed in the text are highlighted according to the following color scheme: blue, active site residues involved in electrostatic interactions with Mg^{2+} and substrate; green, the gating loop catalytic residue; pink and yellow, anchor residue pairs for stabilizing the gating loop; salmon, the residue linking the two anchors; and orange, intraloop interaction. Other invariant residues are typed in green letters.

felt by the phosphoryl group. PPH conserves the loop leucine residue (Leu120) and replaces the mutase Asn122 with an equally polar residue, Thr118. The PPH loop is, therefore, fashioned for closure over the active site.

In the following section, the orientation of the P-pyr and Mg^{+2} cofactor within the PPH active site is analyzed to show that with the exception of correct placement of the active site loop, the crystalline PPH/Mg^{+2}−P-pyr complex depicts a catalytically competent ternary complex.

Active Site. The active site of PPH, crystallized in the presence of 1.8 mM $MgCl_2$ (Mg^{2+} $K_m = 3.5 \pm 0.3$ μM) but without the ligand, failed to show electron density for Mg^{2+}. This same phenomenon was previously reported for MICL (*44*). As was described earlier, P-pyr binding both follows

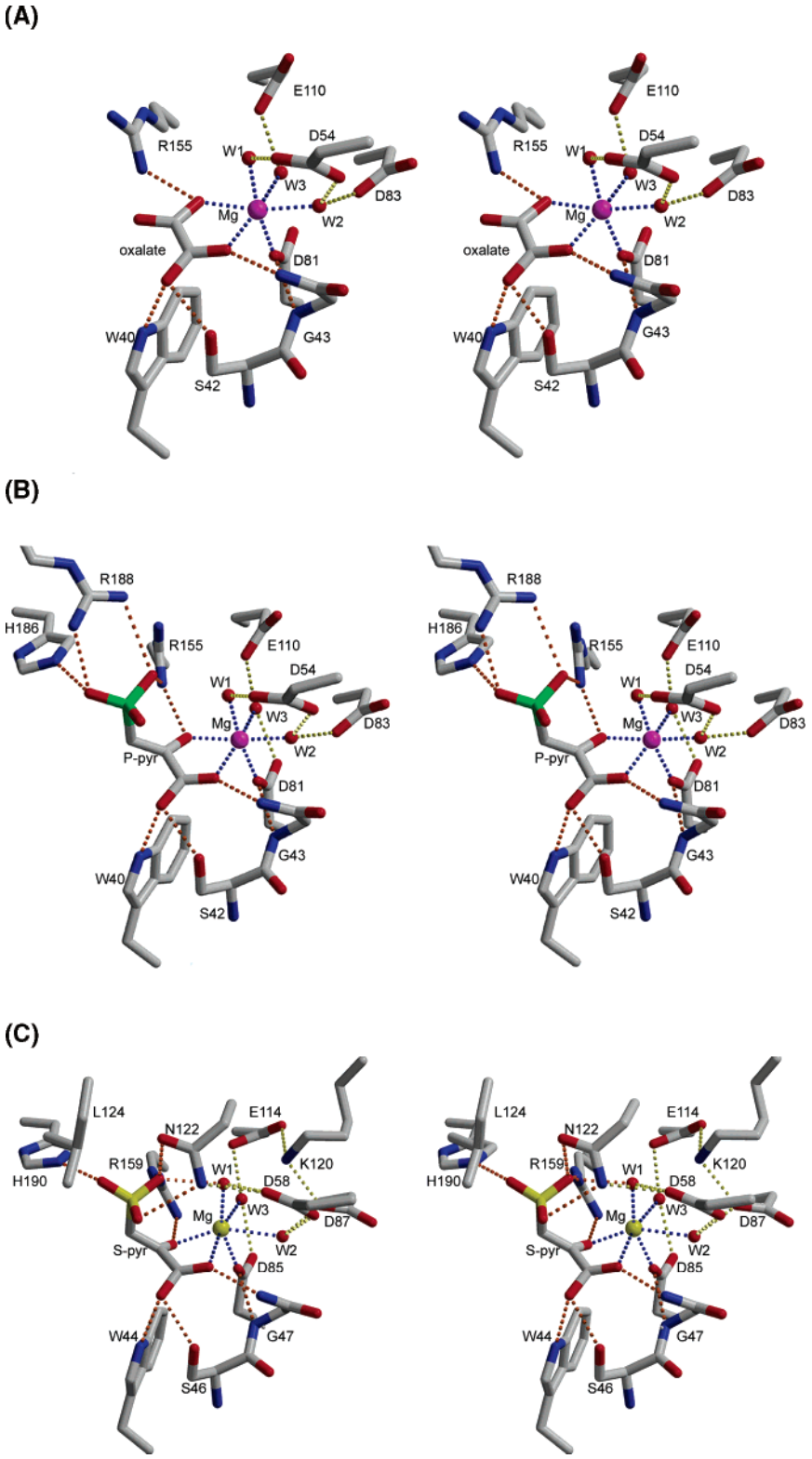

FIGURE 5: Stereoscopic representation of the active site. (A) PPH With bound Mg^{2+}-oxalate and (B) PPH with bound Mg^{2+}-P-pyr. (C) PEPM with bound Mg^{2+}-sulfopyruvate (*43*). Atomic colors are as those in Figure 2 except that carbon is colored gray. Key interactions are highlighted with broken lines as follows: coordination to the Mg^{2+} is shown in blue, protein−water molecule interactions in yellow, and protein−ligand and protein−protein interactions in orange.

and tightens Mg^{2+} binding to PPH, thus accounting for the absence (or disorder) of Mg^{2+} in the active site structure of PPH crystallized without the ligand.

PPH crystals soaked with Mg^{2+} and P-pyr provided a snapshot of the active site with cofactor and substrate bound (Figure 5), which can be compared to the structure of PEPM bound with Mg^{2+} and the P-pyr analogue, sulfopyruvate (*43*). Similarly, PPH crystals grown in the presence of Mg^{2+} and oxalate provide a picture of the active site with cofactor and the stable analogue of the putative pyruvate enolate intermediate bound (Figure 5). This structure can be compared to the structure of the PEPM/Mg^{2+}−oxalate complex (*41*).

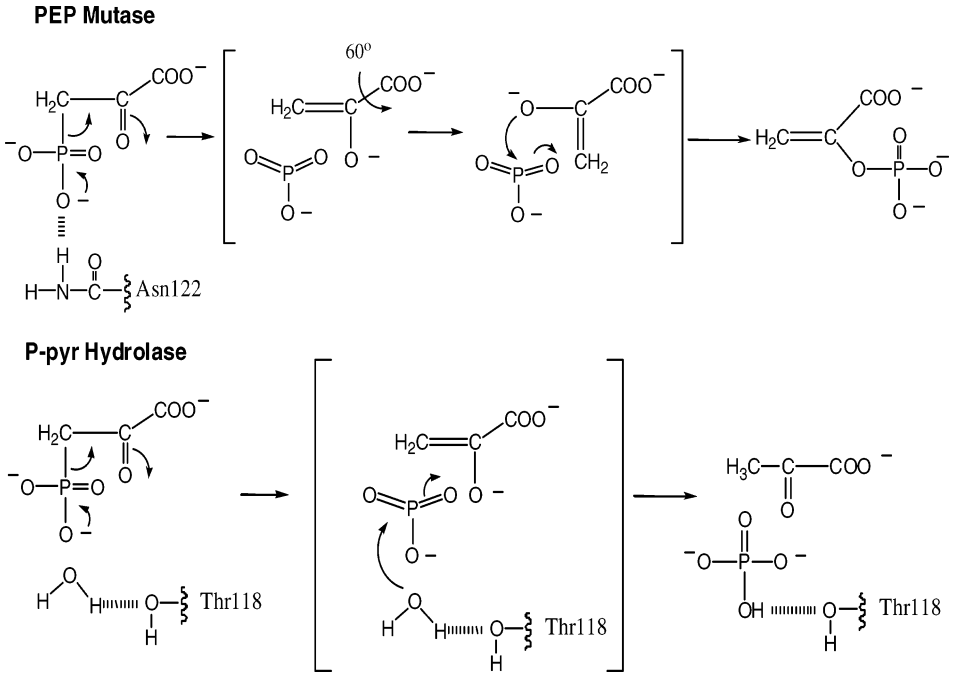

FIGURE 6: Proposed reaction pathways for PEPM and PPH.

On the basis of these structural comparisons, the differences in the active site scaffolds of PEPM and PPH can be identified.

The Mg^{2+}-binding site, which is identical in the two liganded PPH structures, is formed by the carboxylate groups of Asp54, Asp81, Asp83, and Glu110, with Asp81 coordinating directly to the metal, and the remaining carboxylate groups bridged by water molecules (W1, W2, and W3 in Figure 5). The coordination geometry is octahedral, and it is completed by the interaction with the C(1) and C(2) oxygen atoms of P-pyr or oxalate. Of these six coordinating atoms, W2 and W3 are coplanar with the pyruvate/oxalate moiety, and Asp81 Oδ and W1 are perpendicular to the plane. The side chain of Asp83 exhibits two alternate conformations in the oxalate-bound structure. This same constellation of Mg^{2+}-binding residues has been observed in the reported structures of PEPM (*41*, *43*) as well as in the structures of ICL lyase (*45*, *64*, *65*), MICL (*44*, *62*, *63*), and the petal death protein (*61*) (see the sequence alignment of Figure 4).

The carboxylate group of the P-pyr or oxalate ligand interacts with the positive dipoles of the main-chain amide groups of residues 43 and 44 on the *N*-terminal end of the short helix formed by residues 42−50, the side chain hydroxyl group of Ser42, and the side chain Nϵ1 atom of Trp40. An analogous carboxylate-binding motif is present in PEP mutase (Figure 5C) as well as in ICL, MICL, and the petal death protein. On the basis of the multiple sequence alignment of the superfamily members with confirmed function (*44*), the first residue of the carboxylate-binding motif is a serine or threonine (Ser42 in PPH) and the second residue is a glycine (Gly43 in PPH). Other residues are variable (Figure 4). The sequences are, however, conserved within functional families, and there is close agreement between the PEPM consensus sequence, **W**G**SGL**S (residues in bold type are invariant within the PEPM family), and the PPH sequence, WGSGFE.

A pocket lined by the electropositive residues, Arg155, His186 and Arg188, counter the negatively charged phosphono group of the P-pyr bound to PPH (the Arg155 Nζ atom also interacts with O2 of the P-pyr). The same interaction occurs with the O2 of oxalate in the respective PPH complex. Interestingly, in the absence of a phosphono group (free enzyme structure and enzyme/ Mg^{2+}−oxalate complex), the side chain of Arg188 adopts an alternate conformation, interacting with the carbonyl group of Ile160, and is, thus, pointed away from the active site. This change of Arg188 side chain position is associated with main chain conformational changes of residues 186−193 and 258−261. The crystallographic temperature factors of residues 188−190 are high in all three structures, consistent with the implied flexibility of this loop region.

Whereas Arg155 and His186 have counterparts in the PEPM active site (Arg159 and His190, Figure 5), Arg188 does not. Moreover, a comparison of the PPH structure with the closed conformation structure of PEP mutase shows that the interaction of Arg188 with the phosphono group of the P-pyr ligand is possible only when the gating loop adopts an open conformation. Taken together, these data suggest that Arg188 plays no functional role in PPH catalysis and that the observed interaction of the guanidinium group with the phosphono group of P-pyr is incidental. To test this hypothesis, the R188A PPH mutant was prepared for kinetic analysis. The steady-state kinetic constants measured for the R188A PPH mutant, $k_{cat} = 121 \pm 2\ s^{-1}$ (wild-type PPH $k_{cat} = 105\ s^{-1}$) and $K_m = 82 \pm 5\ \mu M$ (wild-type PPH $K_m = 19\ \mu M$), provide conclusive evidence that Arg188 is not required for efficient PPH catalysis. Thus, in the catalytically active conformation of PPH, Arg188 is not positioned to interact with the substrate.

Relationship to PEPM Catalytic Mechanism. In the PPH/ Mg^{2+}−oxalate complex, the C1−C2 torsion angle of the oxalate is 13° off planarity (Figure 5A), whereas in the PPH/ Mg^{2+}−P-pyr complex the C1−C2 torsion angle of the P-pyr

is 31° off planarity (Figure 5B). The oxalate of the PEPM/Mg^{2+}−oxalate complex is planar, and the C1−C2 torsion angle of the pyruvyl moiety of the sulfopyruvate ligand bound in the PEPM/Mg^{2+}−sulfopyruvate complex shows a close to 60° departure from planarity (ref 43 (*43*), Figure 5c). For PEPM, we have proposed a dissociative mechanism involving the formation of metaphosphate and a pyruvate enolate intermediate (Figure 6) (*43*). The oxalate mimics the planar pyruvate enolate intermediate, which at the second step of the reaction undergoes phosphorylation by metaphosphate following a 60º rotation about the pyruvyl C1−C2 bond. This rotation does not alter much the positions of the pyruvyl C2 oxygen and C3 atoms and is possible within the crowded environment of the active site. In contrast, moving the phosphoryl group and keeping the pyruvyl moiety fixed results in clashes with protein groups. The similarity between the active site structure of the PEPM/Mg^{2+}−oxalate complex and that of the PPH/Mg^{2+}−oxalate complex is consistent with the formation of a metaphosphate−pyruvate enolate intermediate in PHH catalysis, yet the hydrolysis does not require rotation around the C1−C2 bond if the water molecule is positioned colinearly with the C3−P bond.

If both PEPM and PHH form a metaphosphate−pyruvate enolate intermediate, then it follows that the PHH active site stations a water molecule for attack, whereas the PEPM active site does not. In PEPM, the residues that interact with the phosphoryl group include His190 and Arg159 (which have the counterparts His186 and Arg155 in PPH), and the active site gating-loop residue Asn122 (Figure 5C). Because the PPH gating loop in the present structures is disordered rather than closed over the active site, we do not have proof that the loop also contributes to binding the P-pyr. Nevertheless, if one assumes that the PPH closed loop adopts the same conformation as that in PEPM (as argued in the previous section), then the PPH counterpart of Asn122 is Thr118. Is it possible that Thr118 stations a water molecule near the P-pyr phosphoryl group in PPH?

The three PPH structures reveal the presence of water molecules in the active site that are absent in the structure of PEPM/ Mg^{2+}−sulfopyruvate. For example, in the structure of the PPH/Mg^{2+}−P-pyr complex, the ligand phosphono group interacts with six water molecules. One water molecule is coordinated to Mg^{2+}, as is the case in PEPM. Each of the remaining five water molecules interacts with protein groups, namely, the side chains of Asp54, Thr213 and Asn236, and the backbone carbonyl group of Gly236. At least some of these water molecules would be expected to be displaced upon loop closure. Two PPH residues that could displace some water molecules are Thr118 and Leu 120 (Asn122 and Leu124 in PEPM), except that the Thr118 side chain is smaller than that of an asparagine. Indeed, because the PPH catalyzes the hydrolysis of P-pyr, we anticipate the retention of at least one water molecule upon loop closure. Assuming that the loop-closed conformation of PPH is the same as that of PEPM, it would be possible for a water molecule to bind between Thr118 hydroxyl group and the phosphono group of P-pyr and be activated for nucleophilic attack. In Figure 6, we have depicted the nucleophilic attack of a Thr118-bound water molecule at the metaphosphate intermediate, concerted with proton transfer to the pyruvate enolate. An alternative reaction mechanism (not shown) is the direct attack of the water at the phosphorus of the bound P-pyr.

Two other active site residues surround P-pyr in the PPH complex and sulfopyruvate in the PEPM complex: PPH Gly235/PEPM Ala239 and PPH Ile273/PEPM Phe277. These, however, do not appear to have substrate-binding or catalytic roles and are probably not responsible for the difference in the catalytic mechanisms of the two enzymes.

CONCLUSION

In PEPM, intramolecular phosphoryl group transfer appears to occur via dissociation to metaphosphate, which alternates between the C(2)O and C(3) of the displaced pyruvate enolate anion (*43*). The active site residues that would function to stabilize the metaphosphate−pyruvate enolate in PEPM are conserved in PHH. The one significant active site residue that is not conserved is Asn122, which in PPH is Thr118. Whereas the Asn122 in PEPM acts as a barrier between the transferring phosphoryl group and solvent, the Thr118 of PPH may bind and polarize a water molecule, thus facilitating the hydrolysis reaction. Presently, it is not clear whether this single amino acid replacement is responsible for the divergence of the PHH from PEPM; however, we expect that future work will resolve this question.

REFERENCES

1. Hildebrand, R. L. (1983) *The Role of Phosphonates in Living Systems*, CRC Press Inc., Boca Raton, FL.
2. Kennedy, K. E., and Thompson, G. A., Jr. (1970) Phosphonolipids: localization in surface membranes of Tetrahymena, *Science 168*, 989−991.
3. Steiner, S., Conti, S. F., and Lester, R. L. (1973) Occurrence of phosphonosphingolipids in Bdellovibrio bacteriovorus strain UKi2, *J. Bacteriol. 116*, 1199−1211.
4. White, R. W., Kemp, P., and Dawson, R. M. (1970) Isolation of a rumen bacterium that hydrogenates oleic acid as well as linoleic acid and linolenic acid, *Biochem. J. 116*, 767−768.
5. Abe, S., Araki, S., Satake, M., Fujiwara, N., Kon, K., and Ando, S. (1991) Structure of triphosphonoglycosphingolipid containing N-acetylgalactosamine 6-O-2-aminoethylphosphonate in the nervous system of Aplysia kurodai, *J. Biol. Chem. 266*, 9939−9943.
6. Hakomori, S. (1990) Bifunctional role of glycosphingolipids. Modulators for transmembrane signaling and mediators for cellular interactions, *J. Biol. Chem. 265*, 18713−18716.
7. Kuzuyama, T., Hidaka, T., Kamigiri, K., Imai, S., and Seto, H. (1992) Studies on the biosynthesis of fosfomycin. 4. The biosynthetic origin of the methyl group of fosfomycin, *J. Antibiot. (Tokyo) 45*, 1812−1814.
8. Horiguchi, M. (1972) Biosynthesis of 2-aminoethylphosphonic acid in cell-free preparations from Tetrahymena, *Biochim. Biophys. Acta. 261*, 102−113.
9. Hara, O., Murakami, T., Imai, S., Anzai, H., Itoh, R., Kumada, Y., Takano, E., Satoh, E., Satoh, A., Nagaoka, K., et al. (1991) The bialaphos biosynthetic genes of Streptomyces viridochromogenes: cloning, heterospecific expression, and comparison with the genes of Streptomyces hygroscopicus, *J. Gen. Microbiol. 137*, 351−359.
10. Bowman, E. D., McQueney, M. S., Barry, R. J., and Dunaway-Mariano, D. (1988) Catalysis and thermodynamics of the phosphoenolpyruvate/phosphonopyruvate rearrangement. Entry into the phosphate class of naturally occurring organophosphorous compounds, *J. Am. Chem. Soc. 110*, 5575−5576.
11. Kim, J., and Dunaway-Mariano, D. (1996) Phosphoenolpyruvate mutase catalysis of phosphoryl transfer in phosphoenolpyruvate: kinetics and mechanism of phosphorus-carbon bond formation, *Biochemistry 35*, 4628−4635.

12. Hildebrand, R. L. (1983) The effects of synthetic phosphonates on living systems, in *The Role of Phosphonates in Living Systems* (Hildebrand, R. L., Ed.), pp 139-169, CRC Press, Inc., Boca Raton, Florida.
13. Baumann, H., Tzianabos, A. O., Brisson, J. R., Kasper, D. L., and Jennings, H. J. (1992) Structural elucidation of two capsular polysaccharides from one strain of Bacteroides fragilis using high-resolution NMR spectroscopy, *Biochemistry 31*, 4081−4089.
14. Araki, S., Abe, S., Yamada, S., Satake, M., Fujiwara, N., Kon, K., and Ando, S. (1992) Characterization of two novel pyruvylated glycosphingolipids containing 2′-aminoethylphosphoryl(→6)-galactose from the nervous system of Aplysia kurodai, *J. Biochem. (Tokyo) 112*, 461−469.
15. Kariotoglou, D. M., and Mastronicolis, S. K. (2001) Sphingophosphonolipids, phospholipids, and fatty acids from Aegean jellyfish Aurelia aurita, *Lipids 36*, 1255−1264.
16. Hard, K., Van Doorn, J. M., Thomas-Oates, J. E., Kamerling, J. P., and Van der Horst, D. J. (1993) Structure of the asn-linked oligosaccharides of apolipophorin III from the insect Locusta migratoria. Carbohydrate-linked 2-aminoethylphosphonate as a constituent of a glycoprotein, *Biochemistry 32*, 766−775.
17. Tamari, M. (1984) C-P Compounds Associated with Peptide, Carbohydrate and Steroid, in *Biochemistry of Natural C-P Compounds* (Hori, T., Horiguchi, M., and Hayashi, A., Eds.), pp 195−200, Maruzen, Ltd., Kyoto, Japan.
18. Barry, R. J., Bowman, E., McQueney, M., and Dunaway-Mariano, D. (1988) Elucidation of the 2-aminoethylphosphonate biosynthetic pathway in Tetrahymena pyriformis, *Biochem. Biophys. Res. Commun. 153*, 177−182.
19. Kittredge, J. S., and Hughes, R. R. (1964) The Occurrence of Alpha-amino-beta-phosphonopropionic acid in the Zoanthid, Zoanthus sociatus, and the ciliate, Tetrahymena pyriformis, *Biochemistry 3*, 991−996.
20. Horigane, A., Horiguchi, M., and Matsumoto, T. (1980) Metabolism of 2-amino-3-phosphono[3-14C]propionic acid in cell-free preparations of Tetrahymena, *Biochim. Biophys. Acta 618*, 383−388.
21. Wackett, L. P., Shames, S. L., Venditti, C. P., and Walsh, C. T. (1987) Bacterial carbon-phosphorus lyase: products, rates, and regulation of phosphonic and phosphinic acid metabolism, *J. Bacteriol. 169*, 710−717.
22. Chen, C. M., Ye, Q. Z., Zhu, Z. M., Wanner, B. L., and Walsh, C. T. (1990) Molecular biology of carbon-phosphorus bond cleavage. Cloning and sequencing of the phn (psiD) genes involved in alkylphosphonate uptake and C-P lyase activity in Escherichia coli B, *J. Biol. Chem. 265*, 4461−4471.
23. Lee, K. S., Metcalf, W. W., and Wanner, B. L. (1992) Evidence for two phosphonate degradative pathways in Enterobacter aerogenes, *J. Bacteriol. 174*, 2501−2510.
24. Wanner, B. L. (1994) Molecular genetics of carbon-phosphorus bond cleavage in bacteria, *Biodegradation 5*, 175−184.
25. Murata, K., Higaki, N., and Kimura, A. (1988) Detection of carbon-phosphorus lyase activity in cell free extracts of Enterobacter aerogenes, *Biochem. Biophys. Res. Commun. 157*, 190−195.
26. Cassaigne, A., Lacoste, A. M., and Neuzil, E. (1976) Research on the catabolism of phosphonic acids: biodegradation of the C-P bond by Pseudomonas aeruginosa, *C. R. Hebd. Seances Acad. Sci., Ser. D 282*, 1637−1639.
27. Jiang, W., Metcalf, W. W., Lee, K. S., and Wanner, B. L. (1995) Molecular cloning, mapping, and regulation of Pho regulon genes for phosphonate breakdown by the phosphonatase pathway of Salmonella typhimurium LT2, *J. Bacteriol. 177*, 6411−6421.
28. La Nauze, J. M., Rosenberg, H., and Shaw, D. C. (1970) The enzymic cleavage of the carbon-phosphorus bond: purification and properties of phosphonatase, *Biochim. Biophys. Acta 212*, 332−350.
29. Parker, G. F., Higgins, T. P., Hawkes, T., and Robson, R. L. (1999) Rhizobium (Sinorhizobium) meliloti phn genes: characterization and identification of their protein products, *J. Bacteriol. 181*, 389−395.
30. Ternan, N. G., and Quinn, J. P. (1998) Phosphate starvation-independent 2-aminoethylphosphonic acid biodegradation in a newly isolated strain of Pseudomonas putida, NG2, *Syst. Appl. Microbiol. 21*, 346−352.
31. Dumora, C., Lacoste, A. M., and Cassaigne, A. (1983) Purification and properties of 2-aminoethylphosphonate:pyruvate aminotransferase from Pseudomonas aeruginosa, *Eur. J. Biochem. 133*, 119−125.
32. Kim, A. D., Baker, A. S., Dunaway-Mariano, D., Metcalf, W. W., Wanner, B. L., and Martin, B. M. (2002) The 2-aminoethylphosphonate-specific transaminase of the 2-aminoethylphosphonate degradation pathway, *J. Bacteriol. 184*, 4134−4140.
33. Morais, M. C., Zhang, W., Baker, A. S., Zhang, G., Dunaway-Mariano, D., and Allen, K. N. (2000) The crystal structure of bacillus cereus phosphonoacetaldehyde hydrolase: insight into catalysis of phosphorus bond cleavage and catalytic diversification within the HAD enzyme superfamily, *Biochemistry 39*, 10385−10396.
34. McGrath, J. W., Wisdom, G. B., McMullan, G., Larkin, M. J., and Quinn, J. P. (1995) The purification and properties of phosphonoacetate hydrolase, a novel carbon-phosphorus bond-cleavage enzyme from Pseudomonas fluorescens 23F, *Eur. J. Biochem. 234*, 225−230.
35. McMullan, G., and Quinn, J. P. (1994) In vitro characterization of a phosphate starvation-independent carbon-phosphorus bond cleavage activity in Pseudomonas fluorescens 23F, *J. Bacteriol. 176*, 320−324.
36. Galperin, M. Y., and Jedrzejas, M. J. (2001) Conserved core structure and active site residues in alkaline phosphatase superfamily enzymes, *Proteins 45*, 318−324.
37. Ternan, N. G., Hamilton, J. T., and Quinn, J. P. (2000) Initial in vitro characterisation of phosphonopyruvate hydrolase, a novel phosphate starvation-independent, carbon-phosphorus bond cleavage enzyme in Burkholderia cepacia Pal6, *Arch. Microbiol. 173*, 35−41.
38. Kulakova, A. N., Wisdom, G. B., Kulakov, L. A., and Quinn, J. P. (2003) The purification and characterization of phosphonopyruvate hydrolase, a novel carbon-phosphorus bond cleavage enzyme from Variovorax sp Pal2, *J. Biol. Chem. 278*, 23426−23431.
39. Ternan, N. G., and Quinn, J. P. (1998) In vitro cleavage of the carbon-phosphorus bond of phosphonopyruvate by cell extracts of an environmental Burkholderia cepacia isolate, *Biochem. Biophys. Res. Commun. 248*, 378−381.
40. Altschul, S. F., Madden, T. L., Schaffer, A. A., Zhang, J., Zhang, Z., Miller, W., and Lipman, D. J. (1997) Gapped BLAST and PSI-BLAST: a new generation of protein database search programs, *Nucleic Acids Res. 25*, 3389−3402.
41. Huang, K., Li, Z., Jia, Y., Dunaway-Mariano, D., and Herzberg, O. (1999) Helix swapping between two alpha/beta barrels: crystal structure of phosphoenolpyruvate mutase with bound Mg(2+)-oxalate, *Structure Fold Des. 7*, 539−548.
42. Liu, S., Lu, Z., Han, Y., Jia, Y., Howard, A., Dunaway-Mariano, D., and Herzberg, O. (2004) Conformational flexibility of PEP mutase, *Biochemistry 43*, 4447−4453.
43. Liu, S., Lu, Z., Jia, Y., Dunaway-Mariano, D., and Herzberg, O. (2002) Dissociative phosphoryl transfer in PEP mutase catalysis: structure of the enzyme/sulfopyruvate complex and kinetic properties of mutants, *Biochemistry 41*, 10270−10276.
44. Liu, S., Lu, Z., Han, Y., Melamud, E., Dunaway-Mariano, D., and Herzberg, O. (2005) Crystal structures of 2-methylisocitrate lyase in complex with product and with isocitrate inhibitor provide insight into lyase substrate specificity, catalysis and evolution, *Biochemistry 44*, 2949−2962.
45. Sharma, V., Sharma, S., Hoener zu Bentrup, K., McKinney, J. D., Russell, D. G., Jacobs, W. R., Jr., and Sacchettini, J. C. (2000) Structure of isocitrate lyase, a persistence factor of Mycobacterium tuberculosis, *Nat. Struct. Biol. 7*, 663−668.
46. Erlich, H. A. (1992) *PCR Technology Principles and Applications for DNA Amplification*, W. H. Freeman and Co., New Work.
47. Appel, R. D., Bairoch, A., and Hochstrasser, D. F. (1994) A new generation of information retrieval tools for biologists: the example of the ExPASy WWW server, *Trends Biochem. Sci. 19*, 258−260.
48. Boggon, T. J., and Shapiro, L. (2000) Screening for phasing atoms in protein crystallography, *Structure Fold Des. 8*, R143−149.
49. Sun, P. D., Radaev, S., and Kattah, M. (2002) Generating isomorphous heavy-atom derivatives by a quick-soak method. Part I: test cases, *Acta Crystallogr., Sect. D 58*, 1092−1098.
50. Otwinowski, Z., and Minor, W. (1997) Processing of x-ray diffraction data collected in oscillation mode, *Methods Enzymol. 276*, 307−326.
51. Navaza, J. (2001) Implementation of molecular replacement in AMoRe, *Acta Crystallogr., Sect. D 57*, 1367−1372.
52. Terwilliger, T. C., and Berendzen, J. (1999) Automated MAD and MIR structure solution, *Acta Crystallogr., Sect. D 55*, 849−861.

53. Terwilliger, T. C. (2000) Maximum-likelihood density modification, *Acta Crystallogr., Sect. D 56*, 965−972.
54. Terwilliger, T. C. (2001) Maximum-likelihood density modification using pattern recognition of structural motifs, *Acta Crystallogr., Sect. D 57*, 1755−1762.
55. Terwilliger, T. C. (2003) Automated main-chain model building by template matching and iterative fragment extension, *Acta Crystallogr., Sect. D 59*, 38−44.
56. Roussel, A., and Cambillau, C. (1989) *Turbo-Frodo*, 4.3 ed., Silicon Graphics Directory, Silicon Graphics, Mountain View, CA.
57. Brünger, A. T., Adams, P. D., Clore, G. M., DeLano, W. L., Gros, P., Grosse-Kunstleve, R. W., Jiang, J. S., Kuszewski, J., Nilges, M., Pannu, N. S., Read, R. J., Rice, L. M., Simonson, T., and Warren, G. L. (1998) Crystallography & NMR system: A new software suite for macromolecular structure determination, *Acta Crystallogr., Sect. D 54*, 905−921.
58. Pannu, N. S., and Read, R. J. (1996) Improved structure refinement through maximum likelihood, *Acta Crystallogr., Sect. A 52*, 659-668.
59. Kim, A., Kim, J., Martin, B. M., and Dunaway-Mariano, D. (1998) Isolation and characterization of the carbon-phosphorus bond-forming enzyme phosphoenolpyruvate mutase from the mollusk Mytilus edulis, *J. Biol. Chem. 273*, 4443−4448.
60. Bowman, E. D., McQueney, M. S., Scholten, J. D., and Dunaway-Mariano, D. (1990) Purification and characterization of the Tetrahymena pyriformis P-C bond forming enzyme phosphoenolpyruvate phosphomutase, *Biochemistry 29*, 7059−7063.
61. Teplyakov, A., Liu, S., Lu, Z., Howard, A., Dunaway-Mariano, D., and Herzberg, O. (2005) Crystal structure of the petal death protein from carnation flower, *Biochemistry 44*, 16377−16384.
62. Simanshu, D. K., Satheshkumar, P. S., Savithri, H. S., and Murthy, M. R. (2003) Crystal structure of Salmonella typhimurium 2-methylisocitrate lyase (PrpB) and its complex with pyruvate and Mg(2+), *Biochem. Biophys. Res. Commun. 311*, 193−201.
63. Grimm, C., Evers, A., Brock, M., Maerker, C., Klebe, G., Buckel, W., and Reuter, K. (2003) Crystal structure of 2-methylisocitrate lyase (PrpB) from Escherichia coli and modelling of its ligand bound active centre, *J. Mol. Biol. 328*, 609−621.
64. Britton, K., Langridge, S., Baker, P. J., Weeradechapon, K., Sedelnikova, S. E., De Lucas, J. R., Rice, D. W., and Turner, G. (2000) The crystal structure and active site location of isocitrate lyase from the fungus Aspergillus nidulans, *Structure Fold Des. 8*, 349−362.
65. Britton, K. L., Abeysinghe, I. S., Baker, P. J., Barynin, V., Diehl, P., Langridge, S. J., McFadden, B. A., Sedelnikova, S. E., Stillman, T. J., Weeradechapon, K., and Rice, D. W. (2001) The structure and domain organization of Escherichia coli isocitrate lyase, *Acta Crystallogr., Sect. D 57*, 1209−1218.
66. Warshel, A. (1998) Electrostatic origin of the catalytic power of enzymes and the role of preorganized active sites, *J. Biol. Chem. 273*, 27035−27038.
67. Cohen, G. H. (1997) ALIGN: a program to superimpose protein coordinates, accounting for insertions and deletions, *J. Appl. Crystallogr. 30*, 1160−1161.
68. Osborne, M. J., Schnell, J., Benkovic, S. J., Dyson, H. J., and Wright, P. E. (2001) Backbone dynamics in dihydrofolate reductase complexes: role of loop flexibility in the catalytic mechanism, *Biochemistry 40*, 9846−9859.
69. Rozovsky, S., Jogl, G., Tong, L., and McDermott, A. E. (2001) Solution-state NMR investigations of triosephosphate isomerase active site loop motion: ligand release in relation to active site loop dynamics, *J. Mol. Biol. 310*, 271−280.
70. Seidel, H. M., and Knowles, J. R. (1994) Interaction of inhibitors with phosphoenolpyruvate mutase: implications for the reaction mechanism and the nature of the active site, *Biochemistry 33*, 5641−5646.

BI061208L